Journal of Materials Chemistry A

ROYAL SOCIETY OF CHEMISTRY

PAPER

View Article Online
View Journal | View Issue

Cite this: J. Mater. Chem. A, 2026, 14, 16784

Electrochemical and computational insights into lithium nucleation at Ni(111) and Cu(111) surfaces for anode-free Li-metal batteries

Katarina Cicvarić,[a] Lars Mannich,[a] Susana Suttor,[ab] Wang Hu,[a] Vitaly Alexandrov[c] and Aliaksandr S. Bandarenka *[a]

The high energy density of anode-free Li-metal batteries (AFLMBs) stems from eliminating the graphite anode, allowing lithium (Li) to be directly electrodeposited onto the current collector during charging. Although copper (Cu) foil is widely employed as a current collector, it often experiences Li dendritic growth, which can cause system failures. Nickel (Ni) foil is a promising alternative as a current collector, meeting the general requirements; however, the in-depth behaviour of Li deposition on Ni remains unclear. Here, we compare the initial stages of Li deposition on model Cu(111) and Ni(111) single crystals by calculating the apparent rate coefficients of Li deposition ($k_{app}(t,E)$). In addition, we apply density functional theory (DFT) calculations to clarify the experimentally observed trends in kinetic parameters. Our results reveal that the overall $k_{app}(t,E)$ on Ni(111) are lower than on Cu(111) with a decreasing trend with increasing overpotential and deposition time. Furthermore, we show that Ni(111) exhibits higher lithiophilicity than Cu(111) as the adsorption energy on the former is lower (more negative values), while exhibiting a similar surface diffusion barrier. A subsequent second layer Li deposition is theoretically examined to have higher adsorption energy on Ni(111) than on Cu(111) for dense configurations, which can facilitate lateral diffusion of Li adatoms, leading to smoother Li growth as shown experimentally. What is more, we show that Ni(111) exhibits higher corrosion resistance, rendering it a preferred material choice as a current collector.

Received 7th January 2026
Accepted 3rd March 2026

DOI: 10.1039/d6ta00180g

rsc.li/materials-a

1. Introduction

Rechargeable batteries are among the most vital innovations of the 21st century, and are critical for a variety of applications, including consumer electronics, electric vehicles, and grid energy storage. Compared to currently dominant commercial lithium (Li)-ion batteries, anode-free Li-metal batteries (AFLMBs) promise enhancement in gravimetric and volumetric energy density.[1] This battery configuration is assembled by coupling a lithiated cathode with a pristine current collector as the anode, separated by a separator infused with liquid carbonate electrolyte. The charging process involves the extraction of Li from the cathode and its electrodeposition as metallic Li onto the current collector, while discharging strips and reinserts it into the cathode. The absence of graphite not only enables higher energy density but also simplifies manufacturing and reduces costs. However, Li easily reacts with components of the electrolyte, forming a so-called solid-electrolyte interphase (SEI) at the electrode/electrolyte interface, causing an irreversible active Li loss and a corresponding capacity loss. Moreover, when charging, Li tends to form highly porous deposits that expose a higher surface area to the electrolyte, and, critically, form needle-like structures called 'dendrites' which can short-circuit the cell, causing thermal runaway and combustion. Consequently, the practical application of this battery configuration has been impeded by poor cycle life and the associated risk of fire.[2–6]

Current collectors in AFLMBs collect electrons released during electrochemical reactions, transport electrons between the electrode materials and the external circuit, extract the thermal energy generated during electrochemical reactions, and serve as substrates for the deposition of metallic Li. General requirements for current collectors are high electronic and thermal conductivity, excellent electrochemical stability, strong corrosion resistance, robust mechanical strength, and cost-efficiency.[7–9] Among the materials that are electrochemically inactive in the operational potential range of the anode (0–3 V *vs.* Li/Li^+) are copper (Cu), nickel (Ni), titanium (Ti), and stainless steel (SS). Electronic conductivity of the proposed materials decreases in the following order: Cu (approx. 59×10^6 S m^{-1}) > Ni (14.4×10^6 S m^{-1}) > Ti (2.5×10^6 S m^{-1}) > SS (1.4×10^6 S

[a]Physics of Energy Conversion and Storage, Department of Physics, Technical University of Munich, James-Franck-Str. 1, Garching, 85748, Germany. E-mail: bandarenka@ph.tum.de

[b]BMW AG, Petuelring 130, 80809 Munich, Germany

[c]Department of Chemical and Biomolecular Engineering, University of Nebraska-Lincoln, 207E Othmer Hall, 68588 Lincoln, NE, USA

m^{-1}), while thermal conductivity in the following order: Cu (approx. 400 W m^{-1} K^{-1}) > Ni (approx. 90 W m^{-1} K^{-1}) > SS (15–25 W m^{-1} K^{-1}) > Ti (approx. 22 W m^{-1} K^{-1}).[10,11] Hence, Cu is the most commonly used current collector owing to its highest electronic and thermal conductivity, while Ni would be the second choice.[12] Ni possesses the highest tensile strength among the suggested materials and the lowest cost (in 2025). Moreover, Ni is more corrosion-resistant than Cu in commercially used carbonate-based organic electrolytes containing $LiPF_6$.[13,14] Despite these advantages, Li electrochemical deposition on Ni remains largely unexplored. However, Cu has been thoroughly investigated at both atomic and macroscopic levels. In this regard, studies at the atomic level have reported surface mobilities and rearrangements on different single crystal Cu facets, showing that Cu(111) favours horizontal and homogeneous growth compared to Cu(110) and Cu(100).[15–17] Diffusion was also studied, with results reporting higher surface diffusion barriers on Cu(001) than on Li(001),[18] hypothesising that surface diffusion at grain boundaries could suppress dendrite formation,[19] and identifying interlayer diffusion as a governing mechanism promoting smooth, dendrite-free films.[20] Pei *et al.* studied the relationship between Li nuclei radius and applied overpotential, finding that lower overpotentials yield larger nuclei, leading to uniform deposition of metallic Li.[21] Regarding the comparison between Cu and Ni, Pande *et al.* performed a thermodynamic analysis of various metal and alloy current collectors, reporting that both Ni(111) and Cu(111) facets have high Li nucleation energy, but the adsorption energy of Li on Ni(111) is lower than that on Cu(111) enabling a lower diffusion energy barrier on Cu(111) than on Ni(111).[22]

Nucleation largely dictates the film growth morphology, where defect sites such as grain boundaries, tips and microcracks provide energetically favourable sites, thereby inducing nonuniform ion flux. This often results in uneven film growth and can lead to the formation of dendrites.[23,24]

In this work, we compare the local deposition kinetics in terms of apparent rate coefficients ($k_{app}(t,E)$) of initial Li electrodeposition on Cu(111) and Ni(111) single crystals, estimated using electrochemical impedance spectroscopy. Here, single crystal Cu and Ni surfaces were chosen to exclude the effect of grain boundaries and defects present in polycrystalline surfaces. In both Cu(111) and Ni(111) cases, a decrease of $k_{app}(t,E)$ with increasing overpotential and deposition time was observed, while the overall $k_{app}(t,E)$ was lower on Ni(111) than on Cu(111). Furthermore, underpotential deposition (UPD) of Li corresponding to $\frac{1}{3}$ of a Li monolayer on Cu(111) and a full monolayer on Ni(111) prior to Li deposition was observed. Density functional theory (DFT) calculations elucidated higher lithiophilicity on Ni(111) than on Cu(111) as the adsorption energy of Li on the former is lower. The simulation of subsequent second layer Li deposition on 1ML Li covered Cu(111) and Ni(111) revealed higher adsorption energy on the latter. This suggests, combined with lower surface diffusion barriers, easier lateral diffusion of Li adatoms on Ni(111) than on Cu(111) when a full monolayer is formed, consequently promoting horizontal Li growth and thereby reducing $k_{app}(t,E)$ as adatoms migrate more easily toward already formed clusters. These insights are in agreement with experiments, where it was observed that Li grains on Ni(111) have a larger area and are smoother than those on Cu(111). Additionally, our experimental findings reveal that the SEI layer on Ni(111) is thinner than that on Cu(111), indicating that Ni is more stable against corrosion. This, coupled with a more uniform initial Li deposition, confirms Ni as a better material for AFLMBs.

2. Results and discussion

2.1 Electrodeposition of Li on Cu(111) and Ni(111) single crystals

During charging, the SEI is formed on the surface of the current collector prior to the deposition of metallic Li. Our previous work started a local kinetic investigation of the early stages of Li deposition on Cu(111) single crystals.[25] Hence, this system was chosen as a benchmark for further investigation and for comparison with Ni(111) under similar conditions. The SEI on Cu(111) and Ni(111) single crystals was formed by applying 10 cycles of cyclic voltammetry (CV) within the potential range of 0–3.55 V *versus* Li/Li^+, as shown in Fig. 1a and b, respectively. Cyclic voltammograms (CVs) were recorded in 1 M $LiPF_6$ in ethylene carbonate : ethyl methyl carbonate (EC : EMC 3 : 7, by wt) with Cu(111) or Ni(111) single crystal as the working electrode, lithium iron phosphate (LFP) as the counter electrode and metallic Li as the reference electrode, starting at OCV, scanning towards 0 V, then back to 3.55 V *vs.* Li/Li^+.

The peaks observed in the first cycle of SEI formation on Cu(111) have been previously identified by Menkin *et al.*: 2.5–3.1 V as CuF_2 reduction resulting in LiF and Cu formation, 2.5–1.5 V as Cu oxide reduction, Cu_xO lithiation and LiF formation, and 0.5 V as reduction of Li_2CO_3 to Li_2C_2 and Li_2O.[26] After the 2nd cycle, a stable SEI is formed, as no significant changes in the CV shape can be observed. The reduction peak at around 0.5 V represents underpotential deposition (UPD) of Li on Cu,[27] while the oxidation peak at around 0.9 V in the reverse scan corresponds to subsequent stripping of the deposited Li. The charge passed for the reduction peak is approximately 100 μC, corresponding to approximately $\frac{1}{3}$ of the Li monolayer. Unlike Cu, the peaks for SEI formation on Ni(111) have not been identified in the literature; however, given the overall shape of the CV, we assume that SEI components are forming, with an additional UPD-related peak at *ca.* 1.0 V. In this case, a stable SEI is formed after the first cycle, as can be seen in Fig. 1b. Here as well, UPD of Li takes place, starting with weak peaks at 2.3, 2.0, 1.1, and 0.8 V, as well as a clearly defined peak at 0.25 V, where the presence of multiple UPD stages represents different modes of adsorption, as already reported.[28] Upon reversing the scan, the oxidation peaks at around 0.5 and 1.6 V represent stripping of the deposited Li. The charge passed for both reduction and oxidation peaks is approximately 300 μC. This corresponds to the formation of a full Li monolayer in the forward scan and a complete stripping in the reverse scan. The detailed derivation and calculation of monolayer coverage on both Cu(111) and Ni(111) can be found in the SI.

The apparent rate coefficient of deposition ($k_{app}(t,E)$) of Li on Cu(111) and Ni(111) is calculated from the following equation,

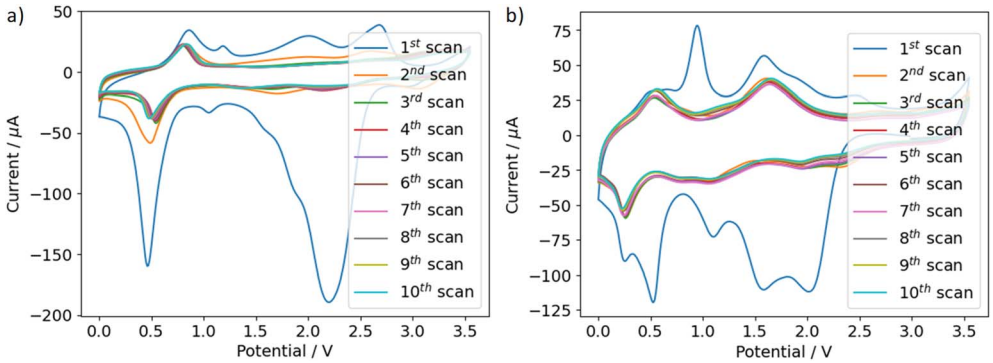

Fig. 1 Ten cyclic voltammetry scans to form the SEI in EC : EMC (3 : 7 by wt) electrolyte with LFP as the counter electrode and Li as the reference electrode on (a) Cu(111) and (b) Ni(111) single crystals.

with a typical Randles-type circuit providing appropriate fitting results:[23]

$$k_{app}(t,E) = \sqrt{2D}\,\frac{A_W(t,E)}{R_{CT}(t,E)} \quad (1)$$

where D represents the diffusion coefficient of the electroactive species, $A_W(t,E)$ is the Warburg coefficient and $R_{CT}(t,E)$ is the charge transfer resistance.

The detailed explanation and derivation of the kinetic parameters can be found in our prior publication.[23] To extract parameters for the calculation of $k_{app}(t,E)$, electrochemical impedance spectroscopy at −5, −10, −15, −20 and −25 mV for 3600 s was carried out. At each potential, 26 impedance spectra were recorded over the course of deposition. The impedance spectra were fitted to the Randles-type equivalent electrical circuit (with parallel RC combination added in series to it to account for the behaviour of the formed SEI) to extract $A_W(t,E)$ and $R_{CT}(t,E)$ for estimating $k_{app}(t,E)$ for Cu(111) and Ni(111) shown as points in Fig. 2a and c, respectively. The figure of 1×10^{-10} m^2 s^{-1} for the diffusion coefficient for Li^+ in EC : EMC is obtained from the literature.[29] Since the depositions were conducted at a constant room temperature (25 °C) at low deposition overpotentials for studying nucleation stages, we assume a constant D for all calculations. Regarding Cu(111), at −5 mV k_{app} increases up to about 300 s, subsequently showing a slight decrease. A distinct behaviour emerges at higher potentials, where k_{app} declines for up to 500 seconds before remaining nearly constant. Fig. 2b shows the average k_{app} calculated after

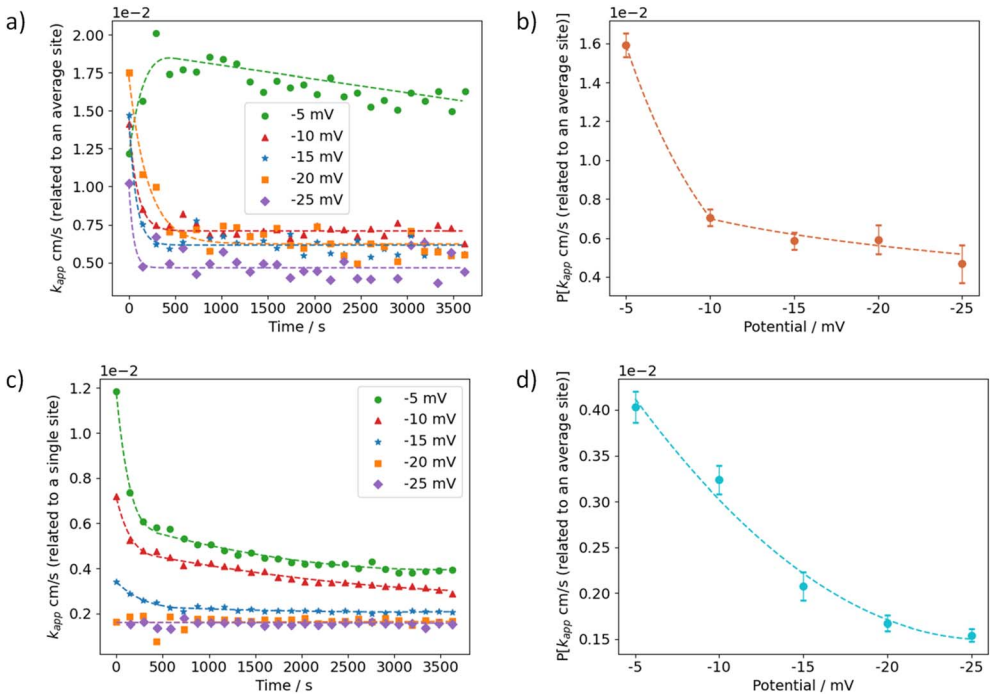

Fig. 2 (a) Dependence of k_{app} for Li deposition on time and potential for Cu(111). (b) Dependence of average k_{app} on deposition potential for Cu(111) after stabilisation (2000 s) with standard deviation as error bars. (c) Dependence of k_{app} for Li deposition on time and potential for Ni(111). (d) Dependence of average k_{app} on deposition potential for Ni(111) after stabilisation (2000 s) with standard deviation as error bars. Dashed lines are visual guides.

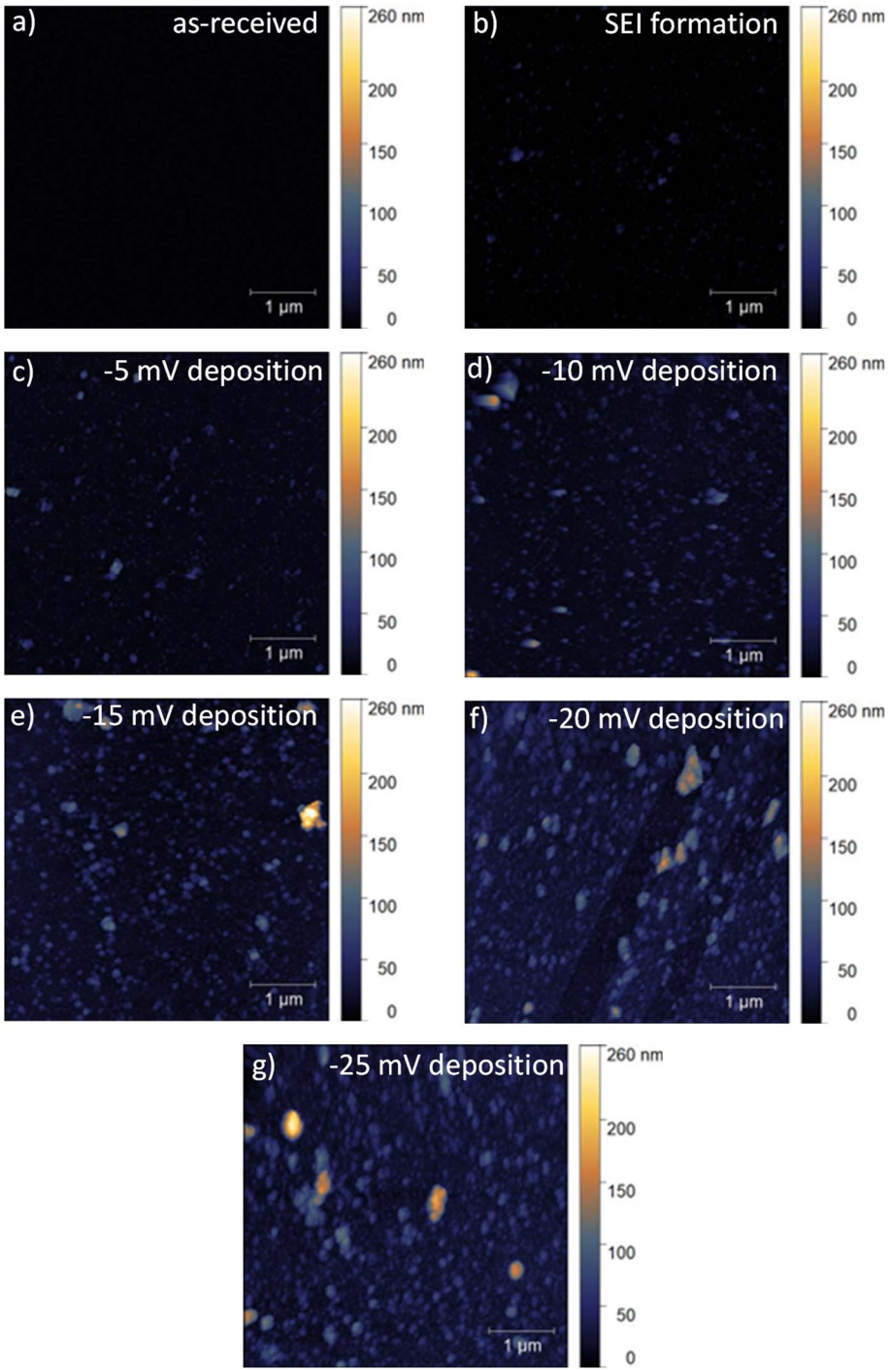

Fig. 3 AFM images of (a) as-received Cu(111) and (b) SEI and Li deposits on the Cu(111) single crystal deposited for 3600 s by EIS at: (c) −5 mV, (d) −10 mV, (e) −15 mV, (f) −20 mV, and (g) −25 mV in EC : EMC (3 : 7 by wt) with LFP as the counter electrode and Li as the reference electrode immersed in EC : EMC (3 : 7, by wt).

stabilisation (after 2000 s) with error bars representing the standard deviation. The most significant drop in k_{app} is noticeable between −5 and −10 mV, whereas between −10 and −25 mV, only a slight change can be observed. In comparison, Ni(111) displays a different behaviour. Here, at potentials between −5 and −15 mV, k_{app} decreases initially up to about 300 s, followed by only a slight decrease at −5 and −10 mV, whereas at −15 mV it remains almost constant. As for −20 and −25 mV, no noticeable change is observed throughout the course of deposition.

It should be noted that the equation for the apparent rate coefficient can be written as follows:[23]

$$k_{app}(t,E) = \frac{n_1 k_{app,1}(t,E) + \ldots + n_i k_{app,i}(t,E)}{n(\text{total})} \quad (2)$$

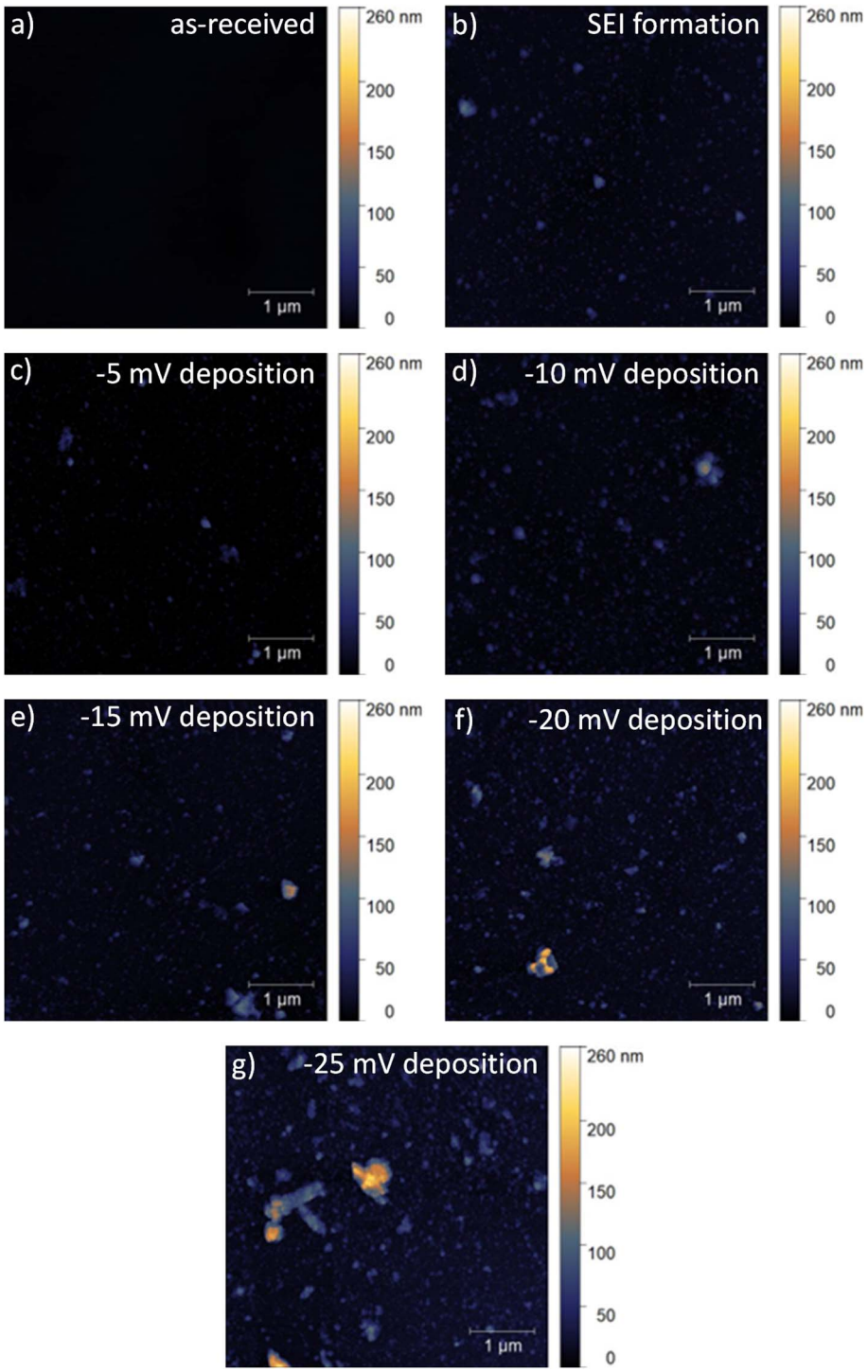

Fig. 4 AFM images of (a) as-received Ni(111) and (b) SEI and Li deposits on the Ni(111) single crystal deposited for 3600 s by EIS at: (c) −5 mV, (d) −10 mV, (e) −15 mV, (f) −20 mV, and (g) −25 mV in EC : EMC (3 : 7 by wt) with LFP as the counter electrode and Li as the reference electrode immersed in EC : EMC (3 : 7, by wt).

where n(total) is the overall number of active Li deposition sites at the surface, and n_1, …, n_i are the numbers of sites with different deposition rates $k_{app,1}(t,E)$, …, $k_{app,i}(t,E)$. Therefore, the observed decrease of the apparent rate coefficient can be explained by the increased contribution of the sites with slower local kinetics (less active sites) with increasing overpotentials or deposition time.[23,30]

The contribution to the reduction in k_{app} from the gradual formation of an ion-depletion region near the electrode surface cannot be neglected. The latter facilitates the movement of ions to more favourable active sites, thereby leading to a decrease in k_{app}.[31] Fig. 2d shows the average k_{app} calculated after 2000 s, showing a decreasing trend with increasing potential. Compared to Cu(111), values of k_{app} are 2 to 4 times lower and

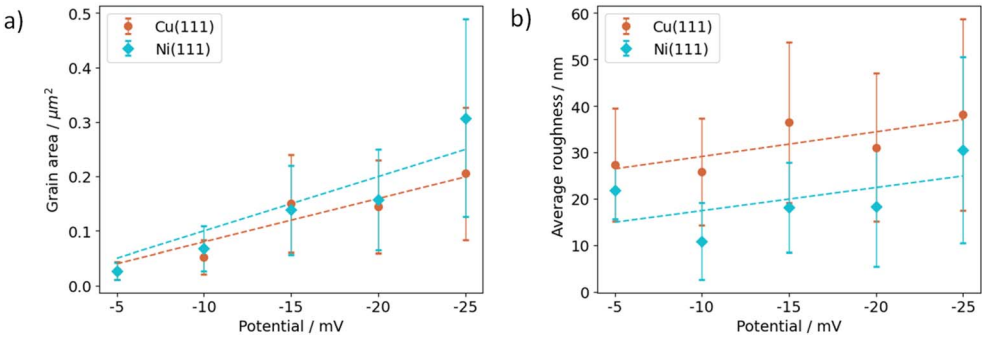

Fig. 5 Dependence of (a) average grain area and (b) average roughness of Li deposits on Cu(111) and Ni(111) at different potentials deposited in a three-electrode cell with LFP as the counter electrode and Li as the reference electrode immersed in EC : EMC (3 : 7, by wt).

show a more linear decrease with increasing potential, unlike Cu, where a significant drop between −5 and −10 mV, followed by a slight decrease at higher potentials can be seen. Fig. 3 and 4 show topographies of Cu(111) and Ni(111) surfaces, respectively. Analysis of surface roughness and grain area was carried out with Gwyddion software,[32] and is shown in Fig. 5. Overall, it can be seen that Li deposits on Cu(111) have a smaller grain size and are rougher than those on Ni(111) (Fig. 5a and b, respectively).

Fig. 6a and b show the SEI capacitance over the course of deposition at different overpotentials on Cu(111) and Ni(111), respectively. Values for SEI capacitance (C_{SEI}) were extracted by fitting 26 impedance spectra recorded during deposition to the proposed electrical equivalent circuit (EEC) detailed in our previous work.[23] The fitting to the suggested EEC (see SI Fig. S1) is good for all measured overpotentials, with RMS deviations typically in the range of a few percent, and is shown in SI (Fig. S2). Regarding Li deposition on Cu(111) (Fig. 6a), SEI capacitance is mainly stable over the course of deposition at all potentials. On comparing different potentials, the largest drop can be seen between −5 and −10 mV, with further decrease from −10 to −15 mV, after which it mostly stabilises at higher overpotentials. Conversely, a different behaviour can be observed on Ni(111) (Fig. 6b), where for −5, −10 and −15 mV a drop can be seen at the beginning of deposition after which it mostly stabilises, whereas at −20 and −25 mV it remains mostly stable over the course of deposition. Overall, SEI capacitance on Cu(111) is lower by two orders of magnitude than that on Ni(111), signifying the formation of a thicker SEI film. Additionally, AFM measurements performed after SEI formation on Cu(111) and Ni(111) (Fig. 3b and 4b, respectively) show average roughness values of approximately 26 nm and 19 nm, respectively. This further supports the conclusion that the SEI film formed on Cu(111) is thicker than that formed on Ni(111). Namely, an increase in the SEI thickness results in a greater distance between the electrode surface and ions, which decreases capacitance.[33] Therefore, it is clear that Ni(111) is more stable in the examined electrolyte system, as it is less prone to decomposition, which can degrade the performance of AFLMBs.[34]

2.2 DFT calculations

We next employed density functional theory (DFT) calculations to further investigate the initial stages of Li electrodeposition on Cu(111) and Ni(111) and to identify possible mechanisms influencing early-stage growth properties. First, the adsorption of a single Li adatom on the pristine current collector surfaces was evaluated. Table 1 shows the adsorption energies of Li at the four symmetrically distinct positions on the fcc(111) facet of both substrate materials. The adsorption energy is significantly lower (more negative values) on Ni(111) at all positions, indicating a higher lithiophilicity than on Cu(111).

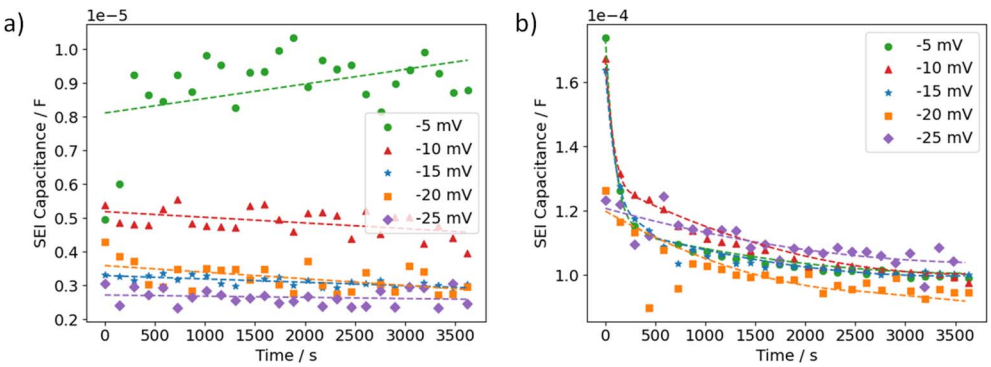

Fig. 6 Dependence of the SEI capacitance on deposition time and potential for (a) Cu(111) and (b) Ni(111) for Li deposition with LFP as the counter electrode and Li as the reference electrode immersed in EC : EMC (3 : 7, by wt).

Table 1 Adsorption energies of a single Li adatom on the pristine Cu(111) and Ni(111) surfaces, placed at the four symmetrically distinct adsorption sites of the fcc(111) facet

	Adsorption energy/eV			
Surface	Top	Bridge	Hollow (hcp)	Hollow (fcc)
Pristine Cu(111)	−2.51	−2.62	−2.63	−2.63
Pristine Ni(111)	−2.79	−2.88	−2.89	−2.89

Table 2 Adsorption energies of a single Li adatom on 1ML Li covered Cu(111) and Ni(111), placed at the four symmetrically distinct adsorption sites of the sustained fcc(111) facet

	Adsorption energy/eV			
Surface	Top	Bridge	Hollow (hcp)	Hollow (fcc)
1ML Li@Cu(111)	−2.06	−2.04	−2.03	−2.04
1ML Li@Ni(111)	−2.03	−2.01	−2.01	−2.01

To investigate the origin of the observed difference in adsorption energies, we further analysed the local electronic structure of Li and the adjacent substrate surface atoms. Fig. 7a and b present the projected density of states (PDOS) for the Cu and Ni systems, respectively. In the case of Ni, the d-band is shifted toward the Fermi level relative to Cu. According to the d-band model proposed by Hammer and Nørskov,[35] this leads to a reduced filling of antibonding states by electrons upon adsorption, thereby increasing the adsorption strength. This may explain the enhanced interaction observed on Ni(111) compared to Cu(111).

To describe further Li deposition on the surfaces of the current collectors, we follow the methodology described in our previous work. Specifically, we evaluated the adsorption strength of Li on the pristine Cu(111) and Ni(111) facets as a function of surface coverage θ. Fig. 8 shows the average adsorption energy calculated for selected coverages, ranging from a single deposited Li atom ($\theta = 0.04$) to a surface completely covered with Li atoms ($\theta = 1$). We find that the adsorption energy is minimal (more negative values) on both substrates with the deposition of an isolated Li atom and gradually increases (less negative values) with subsequent single-layer growth. The most significant change occurs between $\theta = 0.33$ and $\theta = 0.5$, with comparable magnitudes for Cu(111) (+0.29 eV) and Ni(111) (+0.30 eV). This could indicate a transition toward an energetically less favourable close-packed state, the cause of which may lie in the non-negligible lattice mismatch between Li and Cu/Ni. Notably, subsequent deposition after a coverage of $\theta = 0.5$ only results in a minor further change in the adsorption energy (Cu(111): +0.12 eV; Ni(111): +0.20 eV) relative to the preceding deposition (Cu(111): +0.46 eV; Ni(111): +0.50 eV). In general, despite the more pronounced changes on Ni(111) compared to Cu(111), adsorption on Ni(111) remains energetically more favourable regardless of the coverage. This is consistent with the UPD of Li from cyclic voltammetry experiments taking place slightly earlier for the Ni(111) surface (first UPD peak at *ca.* 1.0 V in Fig. 1b) and forming a full monolayer in contrast to an incomplete Li-layer on Cu(111). Furthermore, as lithiophilicity is considered a critical factor in promoting homogeneous nucleation and mitigate dendritic growth,[36,37] it could explain the smoother deposition morphology observed experimentally on Ni(111) (Fig. 5).

Given the experimental observation of Li UPD during SEI formation, we further assume a Li coverage of $\theta = 1$ on the Cu(111) and Ni(111) surfaces to investigate deposition beyond the first layer on both substrates. While this serves only as a rather rough approximation for Cu, since the experimentally

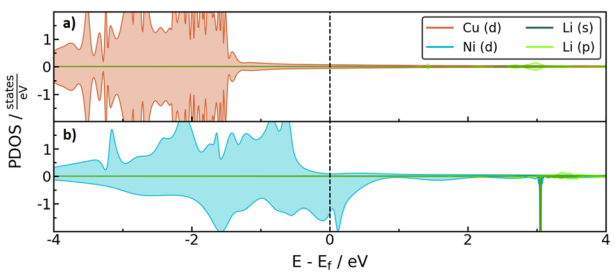

Fig. 7 The projected density of states (PDOS) of an adsorbed, isolated Li atom and adjacent substrate surface layer atoms. (a) Li adatom on the Cu(111) surface and (b) Li adatom on the Ni(111) surface.

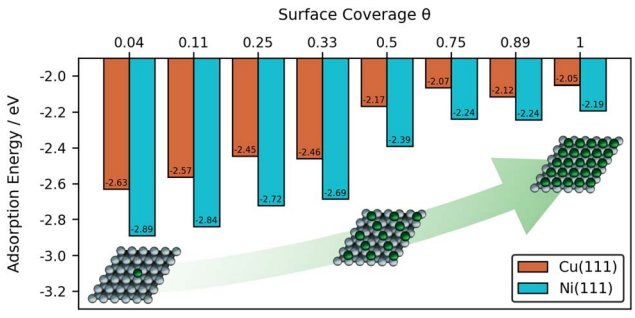

Fig. 8 Average adsorption energy of Li adsorbed on pristine Cu(111) and Ni(111) as a function of surface coverage θ. Substrate atoms are grey, and deposited Li atoms are green.

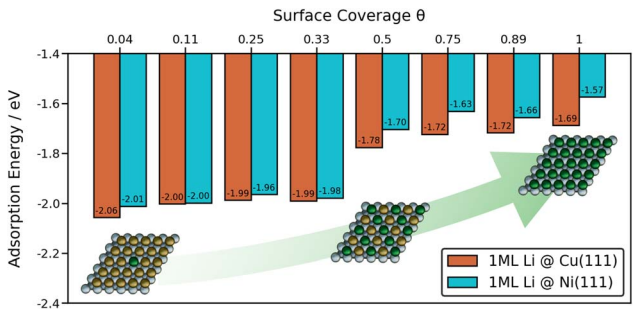

Fig. 9 Average adsorption energy of second-layer Li adsorbed on 1ML covered Cu(111) and Ni(111) as a function of coverage degree θ. Substrate atoms are grey, first-layer Li atoms are yellow and second-layer deposited Li atoms are green.

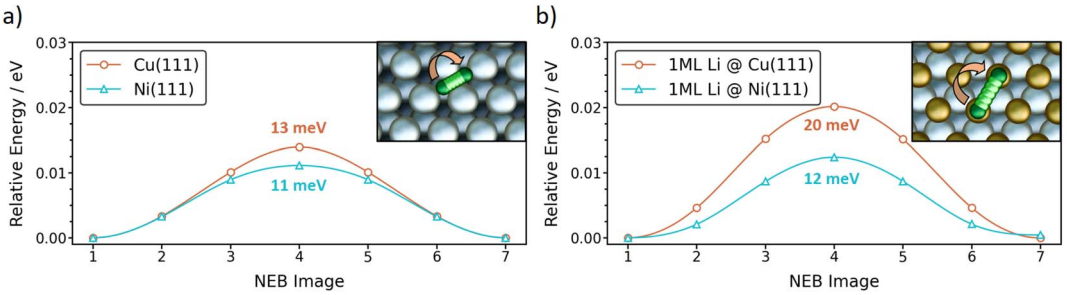

Fig. 10 Surface diffusion energy barriers of Li on (a) pristine Cu(111) and Ni(111) surfaces and (b) 1ML Li covered Cu(111) and Ni(111) surfaces. Substrate atoms are grey, first-layer Li atoms are yellow, evaluated initial and final positions are dark green, and intermediate images are light green.

determined coverage was found to be approximately $\frac{1}{3}$ML, it is in good agreement with the experimental results for Ni. As the hollow sites were identified as the energetically most favourable adsorption sites on both pristine surfaces, UPD monolayer Li atoms were accordingly positioned. The hollow (fcc) sites were selected for simplicity.

To simulate subsequent second-layer deposition, we applied the same methodology as for the first layer. Table 2 shows the calculated adsorption energy of Li placed at the four previously introduced symmetrically distinct positions of the fcc(111) facet. Notably, the adsorption energy has shifted to be nearly equivalent for all sites and almost independent of the underlying substrate. Furthermore, comparison of the adsorption energy between the second-layer Li atom and that of Li atoms in the completed first layer ($\theta = 1$ coverage) reveals no difference on Cu(111), while on Ni(111), the latter is 0.16 eV lower. The lower adsorption strength of the second Li layer could facilitate lateral diffusion of Li adatoms, allowing a horizontal growth pattern during early-stage Li deposition on Ni(111) compared to that on Cu(111). This is supported by experimental data (Fig. 3 and 4), which show smoother, wider grains on Ni(111) than on Cu(111) (Fig. 5).

As the top site was found to be slightly more energetically preferred, the second-layer Li deposition was modelled with Li atoms positioned accordingly. As shown in Fig. 9, the average adsorption energy of second-layer Li remains approximately constant up to a coverage of $\theta = 0.33$, unaltered by the underlying substrate. This behaviour is contrary to the initial changes observed at the onset of deposition for the first layer. However, the transition from $\theta = 0.33$ to $\theta = 0.5$ still results in a significant change in the adsorption energy, further suggesting an energetically less favourable close-packed arrangement. Additionally, the transition is accompanied by a shift toward a more favourable adsorption process on the 1ML Li-covered Cu(111) surface. As this effect is not apparent at low coverages, it may arise from the comparatively smaller lattice mismatch between Cu and Li, leading to reduced compressive strain at higher coverages. As can be seen from Fig. 9, the largest difference in adsorption energies is observed for the full Li coverage on the first lithium monolayer, and adsorption of Li is stronger in the case of the Cu(111) substrate. This can explain the kinetic data that the local deposition apparent rate coefficients are higher in the case of the copper single crystal.

While the adsorption energy serves as a useful indicator of the lithiophilicity of a current collector material, surface diffusion processes are also considered to play a significant role in the ability of a substrate material to promote a horizontal growth mode.[38] As the associated energy barrier decreases, the mobility of the adsorbed species increases and thereby its ability to rearrange and evenly cover the surface, thus favouring horizontal growth over vertical growth. Fig. 10a and b show the surface diffusion barriers of Li on the pristine and the 1ML Li covered Cu(111) and Ni(111) surfaces, respectively. The determined barrier heights for the pristine Cu(111) and Ni(111) surfaces are nearly identical, which disagrees with a lower height on Cu(111) determined by Pande *et al.* using a Brønsted–Evans–Polanyi (BEP) relation between the adsorption enthalpy of 1ML Li covered surfaces and the diffusion energy barrier.[22] However, Kim *et al.* reported a barrier height for Cu(111) that is in very good agreement with our calculations.[16] Furthermore, the results align with our experimental findings: while Ni(111) shows a higher lithiophilicity than Cu(111), surface diffusion processes exhibit similarly low energy barriers, which collectively enhance smoother film growth. At full Li monolayer coverage, the surface diffusion barrier of Li on Cu(111) increases to nearly double that of Ni(111), whereas the latter remains unchanged. This further reinforces the experimentally observed trend of an overall lower apparent coefficient (k_{app}) on Ni(111) than on Cu(111) (Fig. 2), as diffusion of Li adatoms toward already formed clusters is facilitated, leading to more uniform initial growth. However, it should be emphasized that the heights of all calculated energy barriers are relatively small, especially considering that all are found to be lower than the thermal energy at room temperature $k_B T \approx 0.026$ eV. Hence, slow surface diffusion processes may not be the predominant source of dendritic growth on both current collector materials. In addition, we assume a 1ML Li coverage resulting from UPD on both Cu(111) and Ni(111) in our calculations, whereas the experimentally determined coverage is $\frac{1}{3}$ML and 1ML on Cu(111) and Ni(111), respectively. Our calculations reveal a higher adsorption strength on pristine Cu(111) than on 1ML Li-covered Cu(111); hence, an incomplete coverage on Cu(111) further increases the k_{app}.

3. Conclusions

Initial Li deposition on Cu(111) and Ni(111) was studied by EIS at varying potentials to determine a more suitable substrate for anode-free batteries and complemented by DFT calculations to interpret the observed experimental behaviour. DFT calculations reveal that pristine Ni(111) is more lithiophilic than Cu(111), as the adsorption energy of Li on Ni is lower (more negative values) than that on Cu. Experimentally, we observed that UPD of Li occurs on both Cu(111) and Ni(111) prior to Li deposition, forming $\frac{1}{3}$ML and 1ML on Cu(111) and Ni(111), respectively, consistent with DFT calculations. Apparent rate coefficients of deposition ($k_{app}(t,E)$) calculated from fitting EIS spectra to the equivalent electrical circuit show overall higher k_{app} on Cu(111) than on Ni(111), whereas within the same potential k_{app} decreases with time on both Cu(111) and Ni(111). Furthermore, the AFM measurements show more uniform and horizontal Li growth on Ni(111) than on Cu(111) during early-stage deposition. Modelling of second-layer Li deposition on 1ML Li covered Cu(111) and Ni(111) was employed to clarify the experimentally observed trends, revealing lower adsorption energies at coverage degrees $\theta > 0.5$, as well as a higher surface diffusion barrier of Li on Cu than on Ni. This is in accordance with experimental data, as a lower diffusion barrier on 1ML Li covered Ni(111) facilitates lateral diffusion of Li adatoms to already formed clusters, promoting horizontal growth and decreasing k_{app} compared to that of Cu(111). Furthermore, SEI capacitance on Ni(111) is higher than that on Cu(111), indicating the formation of a thinner SEI layer on Ni(111) than on Cu(111), as Ni(111) is more resistant to electrochemical corrosion in the examined electrolyte. Hence, our experimental and simulated data suggest that Ni(111) is preferable to Cu(111) for use in AFLMBs. Nevertheless, current collectors used in practice are polycrystalline foil with imperfections such as grain boundaries and native surface oxide layers. Therefore, the transfer of trends observed on the (111) facet to practical foil should be investigated.

4. Methods

4.1 General

All experiments, including electrochemical measurements and surface topography analysis, were performed in an Ar-filled glovebox (MBraun MB 200B, Germany). The utilized electrolyte was 1 M $LiPF_6$ in ethylene carbonate : ethyl methyl carbonate 3 : 7, by wt (E-Lyte, Germany). As the working electrode, commercially purchased 15 mm diameter × 3 mm thickness Cu(111) or Ni (111) single crystals (MaTeck GmbH, Germany) were used, fixed in an electrochemical cell using a high-density polyethylene holder with a 13 mm diameter opening. For the counter electrode, 14 mm circular discs were punched from commercial 83 μm-thick lithium iron phosphate ($LiFePO_4$)-coated aluminium foil (PI-KEM, UK) and held in place using an HDPE holder with a 12 mm diameter opening. The potentials reported in this study were measured relative to a lithium reference electrode. Following the deposition experiments, the Cu(111) single crystal was carefully rinsed with ethyl methyl carbonate (E-Lyte, Germany) to eliminate any remaining salts. Electrochemical measurements were conducted using a PalmSens4 potentiostat (PalmSens, Netherlands).

4.2 SEI formation and electrochemical impedance spectroscopy (EIS)

Before initiating the Li deposition experiments, a stable solid-electrolyte interface was formed by cyclic voltammetry over 10 scans in the potential range from 3.55 to 0 V *vs.* Li/Li^+ at a scan rate of 50 mV s^{-1}. In EIS measurements, small ac signals with 1 mV amplitude were used. The frequency range explored spanned 0.1 Hz to 100 kHz, employing a time-scan method over 3600 seconds for each overpotential, resulting in the acquisition of 26 impedance spectra for each overpotential. The analysis of the EIS spectra was conducted using Kramers–Kronig relation verification, circuit modelling, and parameter extraction, utilizing the EIS Spectrum Analyser software.[39] After deposition, a cyclic voltammogram was obtained in a potential range between 3.55 and 0 V *vs.* Li/Li^+ to identify the oxidation peak associated with Li stripping. The deposited Li was subsequently stripped by applying the oxidation potential.

4.3 Surface topography

Surface topography was analysed using tapping mode atomic force microscopy (AFM) (Multimode 8, Bruker, USA). AFM images were captured utilizing a NCHV probe (Bruker, USA) with a spring constant of 42 N m^{-1} at a scanning rate of 0.1 Hz.

4.4 Computational details

Density functional theory (DFT) calculations simulating atomic scale deposition of Li atoms onto Cu(111) and Ni(111) surfaces were performed using the Vienna *ab initio* simulation package (VASP) code.[40,41] The generalized gradient approximation (GGA) Perdew–Burke–Ernzerhof (PBE) exchange–correlation functional[42] was applied together with the projector augmented wave (PAW)[43,44] pseudopotentials for Li, Cu and Ni to represent core electrons. The total energy of all systems was found to be converged with a plane-wave basis set kinetic cut-off energy of 500 eV. The self-consistent field (SCF) convergence criterion was set to 10^{-6} eV. All geometries were relaxed to forces below 10^{-2} eV $Å^{-1}$. Lattice constants used to construct the Cu(111) and Ni(111) slabs were calculated to be 3.63 Å and 3.52 Å, which are in very good agreement with other DFT calculated values.[45,46] Spin-polarized calculations were performed for all Ni systems to account for the magnetic properties. The van der Waals dispersion energy-correction method DFT-D3 (ref. 47) was used with the Becke–Johnson damping function[48] for all adsorption energy and surface diffusion calculations. Slab supercells exposing the (111) facet along the *z*-direction were constructed with sizes of $p(2 \times 2)$, $p(3 \times 3)$ and $p(5 \times 5)$ in the *x*–*y*-plane. The respective Brillouin zones were sampled using Gamma-centered *k*-point grids with dimensions of $13 \times 13 \times 1$, $9 \times 9 \times 1$ and $5 \times 5 \times 1$. A vacuum region of 15 Å along the *z*-direction was introduced to prevent interactions between neighbouring periodic images. The surface energies of Cu(111) and Ni(111) were found to be converged to values of 1.31 J m^{-2} and 1.92 J m^{-2}

with a slab thickness of five layers, which is in good agreement with other DFT calculated values.[49–51] The uppermost three Cu/Ni substrate layers were allowed to relax for all calculations. Adsorbed Li was allowed to relax only along the *z*-direction when evaluating the adsorption energy at different positions, and along all directions when evaluating different coverages. The adsorption energies were calculated as follows:

$$E_{ads} = E_{n\mathrm{Li@surf}} - E_{surf} - n \times E_{Li}$$

where $E_{n\mathrm{Li@surf}}$, E_{surf}, E_{Li} and n are the total energies calculated using DFT, extrapolated to 0 K, for the surface with n adsorbed Li atoms, without the Li atoms, and the single Li atom, respectively. Surface diffusion energy barriers were determined within supercell systems of size $p(5 \times 5)$ using the climbing image Nudged Elastic Band (CI-NEB) method with five images along the respective paths.[52–55]

Conflicts of interest

There are no conflicts to declare.

Data availability

The data that support the findings of this study are available from the corresponding author upon reasonable request.

Supplementary information (SI): monolayer coverage derivation and calculation on Cu(111) and Ni(111); suggested equivalent electric circuit (EEC) modelling the interface during electrodeposition of Li on Cu(111) and Ni(111) surfaces; electrochemical impedance spectra of electrodeposition of Li at different potentials with the corresponding fittings to the suggested EEC. See DOI: https://doi.org/10.1039/d6ta00180g.

Acknowledgements

This research is funded by the DFG (Excellence Cluster "e-conversion", Excellence Strategy – EXC 2089/1 – 390776260), with additional credit given to the Technical University of Munich (TUM) for the Laura Bassi scholarship.

References

1 L. Lin, K. Qin, Y. sheng Hu, H. Li, X. Huang, L. Suo and L. Chen, A Better Choice to Achieve High Volumetric Energy Density: Anode-Free Lithium-Metal Batteries, *Adv. Mater.*, 2022, **34**(23), 2110323, DOI: 10.1002/adma.202110323.

2 S. Nanda, A. Gupta and A. Manthiram, Anode-Free Full Cells: A Pathway to High-Energy Density Lithium-Metal Batteries, *Adv. Energy Mater.*, 2021, **11**(2), 2000804, DOI: 10.1002/aenm.202000804.

3 Z. Xie, Z. Wu, X. An, X. Yue, J. Wang, A. Abudula and G. Guan, Anode-free rechargeable lithium metal batteries: progress and prospects, *Energy Storage Mater.*, 2020, **32**, 386–401, DOI: 10.1016/j.ensm.2020.07.004.

4 J. Qian, B. D. Adams, J. Zheng, W. Xu, W. A. Henderson, J. Wang and J. G. Zhang, Anode-Free Rechargeable Lithium Metal Batteries, *Adv. Funct. Mater.*, 2016, **26**(39), 7094–7102, DOI: 10.1002/adfm.201602353.

5 R. V. Salvatierra, W. Chen and J. M. Tour, What Can be Expected from "Anode-Free" Lithium Metal Batteries?, *Adv. Energy Sustain. Res.*, 2021, **2**(5), 2000110, DOI: 10.1002/aesr.202000110.

6 S. Huo, L. Wang, B. Su, W. Xue, Y. Wang, H. Zhang and X. He, Anode-Free Li Metal Batteries: Feasibility Analysis and Practical Strategy, *Adv. Mater.*, 2024, **36**(47), 2411757, DOI: 10.1002/adma.202411757.

7 Q. Shi, C. Lu, Y. Cao, Y. Hao, A. Bachmatiuk and M. H. Rümmeli, Recent developments in current collectors for lithium metal anodes, *Mater. Chem. Front.*, 2023, **7**(7), 1298–1311, DOI: 10.1039/d3qm00029j.

8 Y. Zhang, S. Jing, H. Shen, S. Li, Y. Huang, Y. Shen and F. Liu, Developments, Novel Concepts, and Challenges of Current Collectors: From Conventional Lithium Batteries to All-Solid-State Batteries, *ChemElectroChem*, 2024, **11**(4), e202300739, DOI: 10.1002/celc.202300739.

9 C. Lamiel, I. Hussain, X. Ma and K. Zhang, Properties, functions, and challenges: current collectors, *Mater. Today Chem.*, 2022, **26**, 101152, DOI: 10.1016/j.mtchem.2022.101152.

10 https://steelprogroup.com/stainless-steel/properties/thermal-conductivity/.

11 D. R. Lide, *CRC Handbook of Chemistry and Physics*, 84th edn, 2003.

12 S. Rezaee, H. Araghi, H. Noshad and Z. Zabihi, Physical characteristics of nickel thin-films and nickel thin-film foams as Li-air batteries anode and cathode current collectors, *J. Mol. Liq.*, 2023, **383**, 122171, DOI: 10.1016/j.molliq.2023.122171.

13 K. Cho, J. Baek, C. Balamurugan, H. Im and H. J. Kim, Corrosion study of nickel-coated copper and chromate-coated aluminum for corrosion-resistant lithium-ion battery lead-tab, *J. Ind. Eng. Chem.*, 2022, **106**, 537–545, DOI: 10.1016/j.jiec.2021.11.028.

14 Y. Liu, D. Gao, H. Xiang, X. Feng and Y. Yu, Research Progress on Copper-Based Current Collector for Lithium Metal Batteries, *Energy Fuels*, 2021, **35**(16), 12921–12937, DOI: 10.1021/acs.energyfuels.1c02008.

15 G. Lai, J. Jiao, C. Fang, Y. Jiang, L. Sheng, B. Xu and J. Zheng, The Mechanism of Li Deposition on the Cu Substrates in the Anode-Free Li Metal Batteries, *Small*, 2023, **19**(3), 2205416, DOI: 10.1002/smll.202205416.

16 M. H. Kim, D. Y. Kim, Y. Li, J. Kim, M. H. Kim, J. Seo and H. W. Lee, Horizontal lithium growth driven by surface dynamics on single crystal Cu(111) foil, *Energy Environ. Sci.*, 2024, **17**(18), 6521–6532, DOI: 10.1039/d4ee01766h.

17 G. Li, D. Shi, Z. Hao, Y. Lu, Q. Zhao, Z. Yan and J. Chen, Computational Insights into the Crystal Facet Selectivity of Cu Current Collector for the Growth of Lithium Metal, *J. Phys. Chem. C*, 2023, **127**(33), 16297–16303, DOI: 10.1021/acs.jpcc.3c03096.

18 I. T. Røe and S. K. Schnell, Slow surface diffusion on Cu substrates in Li metal batteries, *J. Mater. Chem. A*, 2021, **9**(17), 11042–11048, DOI: 10.1039/d1ta02300d.
19 A. A. Rulev, Y. O. Kondratyeva, L. V. Yashina and D. M. Itkis, Lithium Planar Deposition vs Whisker Growth: Crucial Role of Surface Diffusion, *J. Phys. Chem. Lett.*, 2020, **11**(24), 10511–10518, DOI: 10.1021/acs.jpclett.0c02674.
20 B. S. Vishnugopi, F. Hao, A. Verma and P. P. Mukherjee, Surface diffusion manifestation in electrodeposition of metal anodes, *Phys. Chem. Chem. Phys.*, 2020, **22**(20), 11286–11295, DOI: 10.1039/d0cp01352h.
21 A. Pei, G. Zheng, F. Shi, Y. Li and Y. Cui, Nanoscale Nucleation and Growth of Electrodeposited Lithium Metal, *Nano Lett.*, 2017, **17**(2), 1132–1139, DOI: 10.1021/acs.nanolett.6b04755.
22 V. Pande and V. Viswanathan, Computational Screening of Current Collectors for Enabling Anode-Free Lithium Metal Batteries, *ACS Energy Lett.*, 2019, **4**(12), 2952–2959, DOI: 10.1021/acsenergylett.9b02306.
23 J. Qiu, R. Qiu, Z. Mao, Y. Han, P. Madhusudan, X. Wang, C. Wang, C. Qi, X. Yu, S. Zeng, *et al.*, A review on copper current collector used for lithium metal batteries: challenges and strategies, *J. Energy Storage*, 2024, **100**, 113683, DOI: 10.1016/j.est.2024.113683.
24 X. Guan, A. Wang, S. Liu, G. Li, F. Liang, Y.-W. Yang, X. Liu and J. Luo, Controlling Nucleation in Lithium Metal Anodes, *Small*, 2018, **14**(37), 1801423.
25 K. Cicvarić, L. Mannich, D. Blum, W. Hu, S. Suttor, V. Alexandrov and A. S. Bandarenka, Electrochemical and Computational Insights into Lithium Nucleation on Single Crystal Copper for Anode-free Li-metal Batteries, *J. Phys. Chem. C*, 2026, **130**(2), 1096–1104, DOI: 10.1021/acs.jpcc.5c07557.
26 S. Menkin, C. A. Okeefe, A. B. Gunnarsdóttir, S. Dey, F. M. Pesci, Z. Shen, A. Aguadero and C. P. Grey, Toward an Understanding of SEI Formation and Lithium Plating on Copper in Anode-Free Batteries, *J. Phys. Chem. C*, 2021, **125**(30), 16719–16732, DOI: 10.1021/acs.jpcc.1c03877.
27 S. T. Liu, H. Y. Ku, C. L. Huang and C. C. Hu, Improvements in Li deposition and stripping induced by Cu (111) nanotwinned columnar grains, *Electrochim. Acta*, 2022, **430**, 141011, DOI: 10.1016/j.electacta.2022.141011.
28 L. F. Li, D. Totir, Y. Gofer, G. S. Chottiner and D. A. Scherson, The electrochemistry of nickel in a lithium-based solid polymer electrolyte in ultrahigh vacuum environments, *Electrochim. Acta*, 1998, **44**(6–7), 949–955, DOI: 10.1016/S0013-4686(98)00198-4.
29 C. Capiglia, Y. Saito, H. Kageyama, P. Mustarelli, T. Iwamoto, T. Tabuchi and H. Tukamoto, ^{7}Li and ^{19}F diffusion coefficients and thermal properties of non-aqueous electrolyte solutions for rechargeable lithium batteries, *J. Power Sources*, 1999, **81**, 859–862, DOI: 10.1016/S0378-7753(98)00237-7.
30 B. B. Berkes, J. B. Henry, M. Huang and A. S. Bondarenko, Electrochemical characterisation of copper thin film formation on polycrystalline platinum, *ChemPhysChem*, 2012, **13**, 3210–3217, DOI: 10.1002/cphc.201200193.
31 K. Cicvarić, S. Pohlmann, B. Zhang, F. Rahmanian, L. Merker, M. Gaberšček and H. S. Stein, Fast formation of anode-free Li-metal batteries by pulsed current, *Phys. Chem. Chem. Phys.*, 2024, **26**(20), 14713–14720, DOI: 10.1039/d4cp00775a.
32 D. Nečas and P. Klapetek, Gwyddion: an open-source software for SPM data analysis, *Cent. Eur. J. Phys.*, 2012, **10**(1), 181–188, DOI: 10.2478/s11534-011-0096-2.
33 M. Schalenbach, B. Wu, C. L. Tsai, A. Windmüller, L. Raijmakers, S. Yu, H. Tempel and R. A. Eichel, Double layer capacitance as a sensitive metric to monitor the formation of solid electrolyte interphases in Li-ion batteries, *Energy Adv.*, 2024, **4**(1), 140–151, DOI: 10.1039/d4ya00524d.
34 C. Wang, L. Wu, Y. Hong, Y. Zhang, S. Wang, G. Zhou, Z. Wen, W. He, H. Han and Y. Xu, Preventing anode degradation through copper foil surface modification techniques for lithium-ion batteries, *Surf. Interfaces*, 2025, **72**, 107240, DOI: 10.1016/j.surfin.2025.107240.
35 B. Hammer and J. K. Nørskov, Why gold is the noblest of all the metals, *Nature*, 1995, **376**(6537), 238–240, DOI: 10.1038/376238a0.
36 K. Yan, Z. Lu, H. W. Lee, F. Xiong, P. C. Hsu, Y. Li, J. Zhao, S. Chu and Y. Cui, Selective deposition and stable encapsulation of lithium through heterogeneous seeded growth, *Nat. Energy*, 2016, **1**, 16010, DOI: 10.1038/nenergy.2016.10.
37 D. Petersen, M. Gronenberg, G. Lener, E. P. Leiva, G. L. Luque, S. Rostami, A. Paolella, B. J. Hwang, R. Adelung and M. Abdollahifar, Anode-free post-Li metal batteries, *Mater. Horiz.*, 2024, **11**(23), 5914–5945, DOI: 10.1039/D4MH00529E.
38 M. Jäckle, K. Helmbrecht, M. Smits, D. Stottmeister and A. Groß, Self-diffusion barriers: possible descriptors for dendrite growth in batteries?, *Energy Environ. Sci.*, 2018, **11**(12), 3400–3407, DOI: 10.1039/C8EE01448E.
39 A. S. Bandarenka, Development of hybrid algorithms for EIS data fitting, in *Lecture Notes on Impedance Spectroscopy. Measurement, Modelling and Applications*, ed. O. Kanoun, CRC Press, Tailor and Francis Group, 2013, vol. 4, pp. 29–36.
40 G. Kresse and J. Furthmüller, Efficiency of ab-initio total energy calculations for metals and semiconductors using a plane-wave basis set, *Comput. Mater. Sci.*, 1996, **6**(1), 15–50, DOI: 10.1016/0927-0256(96)00008-0.
41 G. Kresse and J. Furthmüller, Efficient iterative schemes for ab initio total-energy calculations using a plane-wave basis set, *Phys. Rev. B:Condens. Matter Mater. Phys.*, 1996, **54**(16), 11169–11186, DOI: 10.1103/PhysRevB.54.11169.
42 J. P. Perdew, K. Burke and M. Ernzerhof, Generalized Gradient Approximation Made Simple, *Phys. Rev. Lett.*, 1996, **77**(18), 3865–3868, DOI: 10.1103/PhysRevLett.77.3865.
43 P. E. Blöchl, Projector augmented-wave method, *Phys. Rev. B:Condens. Matter Mater. Phys.*, 1994, **50**(24), 17953–17979, DOI: 10.1103/PhysRevB.50.17953.
44 G. Kresse and D. Joubert, From ultrasoft pseudopotentials to the projector augmented-wave method, *Phys. Rev. B:Condens.*

Matter Mater. Phys., 1999, **59**(3), 1758–1775, DOI: 10.1103/PhysRevB.59.1758.

45 P. Haas, F. Tran and P. Blaha, Calculation of the lattice constant of solids with semilocal functionals, *Phys. Rev. B:Condens. Matter Mater. Phys.*, 2009, **79**(8), 085104, DOI: 10.1103/PhysRevB.79.085104.

46 A. Jain, *et al.*). The materials project: a materials genome approach to accelerating materials innovation, *APL Mater.*, 2013, **1**(1), 011002, DOI: 10.1063/1.4812323.

47 S. Grimme, J. Antony, S. Ehrlich and H. Krieg, A consistent and accurate *ab initio* parametrization of density functional dispersion correction (DFT-D) for the 94 elements H-Pu, *J. Chem. Phys.*, 2010, **132**(15), 154104, DOI: 10.1063/1.3382344.

48 S. Grimme, S. Ehrlich and L. Goerigk, Effect of the damping function in dispersion corrected density functional theory, *J. Comput. Chem.*, 2011, **32**(7), 1456–1465, DOI: 10.1002/jcc.21759.

49 R. Tran, Z. Xu, B. Radhakrishnan, *et al.*) Surface energies of elemental crystals, *Sci. Data*, 2016, **3**, 160080, DOI: 10.1038/sdata.2016.80.

50 V. Pande and V. Viswanathan, Computational screening of current collectors for enabling anode-free lithium metal batteries, *ACS Energy Lett.*, 2019, **4**(12), 2952–2959.

51 J. H. Montoya and K. A. Persson, A high-throughput framework for determining adsorption energies on solid-surfaces, *npj Comput. Mater.*, 2017, **3**(1), 14, DOI: 10.1038/s41524-017-0017-z.

52 G. Mills, H. Jónsson and G. K. Schenter, Reversible work transition state theory: application to dissociative adsorption of hydrogen, *Surf. Sci.*, 1995, **324**(2–3), 305–337, DOI: 10.1016/0039-6028(94)00731-4.

53 H. Jónsson, G. Mills and K. W. Jacobsen, Nudged elastic band method for finding minimum energy paths of transitions, *Classical and Quantum Dynamics in Condensed Phase Simulations*, 1998, pp. 385–404, DOI: 10.1142/9789812839664_0016.

54 G. Henkelman, B. P. Uberuaga and H. Jónsson, A climbing image nudged elastic band method for finding saddle points and minimum energy paths, *J. Chem. Phys.*, 2000, **113**(22), 9901–9904, DOI: 10.1063/1.1329672.

55 G. Henkelman and H. Jónsson, Improved tangent estimate in the nudged elastic band method for finding minimum energy paths and saddle points, *J. Chem. Phys.*, 2000, **113**(22), 9978–9985, DOI: 10.1063/1.1323224.